



Tomography of time-dependent quantum Hamiltonians with machine learningChen-Di Han ¹, Bryan Glaz,² Mulugeta Haile,² and Ying-Cheng Lai ^{1,3,*}¹*School of Electrical, Computer and Energy Engineering, Arizona State University, Tempe, Arizona 85287, USA*²*Vehicle Technology Directorate, CCDC Army Research Laboratory, 2800 Powder Mill Road, Adelphi, Maryland 20783-1138, USA*³*Department of Physics, Arizona State University, Tempe, Arizona 85287, USA*

(Received 9 April 2021; revised 24 September 2021; accepted 8 November 2021; published 1 December 2021)

Interacting quantum Hamiltonians are fundamental to quantum computing. Data-based tomography of time-independent quantum Hamiltonians has been achieved, but an open challenge is to ascertain the structures of time-dependent quantum Hamiltonians using time series measurements taken locally from a small subset of the spins. Physically, the dynamical evolution of a spin system under time-dependent driving or perturbation is described by the Heisenberg equation of motion. Motivated by this basic fact, we articulate a physics-enhanced machine-learning framework whose core is Heisenberg neural networks. In particular, we develop a deep learning algorithm according to some physics-motivated loss function based on the Heisenberg equation, which “forces” the neural network to follow the quantum evolution of the spin variables. We demonstrate that, from local measurements, not only can the local Hamiltonian be recovered, but the Hamiltonian reflecting the interacting structure of the whole system can also be faithfully reconstructed. We test our Heisenberg neural machine on spin systems of a variety of structures. In the extreme case in which measurements are taken from only one spin, the achieved tomography fidelity values can reach about 90%. The developed machine-learning framework is applicable to any time-dependent systems whose quantum dynamical evolution is governed by the Heisenberg equation of motion.

DOI: [10.1103/PhysRevA.104.062404](https://doi.org/10.1103/PhysRevA.104.062404)**I. INTRODUCTION**

Quantum computation based on spin is a fundamental component of quantum information science and technology [1]. Recently, it has been demonstrated that manipulating 50 spins can generate a computational capability beyond any kind of classical computers, leading to quantum supremacy [2,3]. From a network point of view, the information exchange between any pair of spins can be regarded as a link between the two spins. When the interactions associated with all spin pairs are taken into account, the end result is effectively a network, giving rise to a subfield called a qubit or a spin system [4–6]. Experimentally, a multispin coupling system can be realized using cavity quantum electrodynamics [7], ion traps [8], or superconducting qubits [2,3].

There are two types of quantum Hamiltonians: time-independent or time-dependent. In the former case, the system can be decomposed into a sequence of quantum gates [9], resembling a classical circuit structure. Since the Hamiltonian is constant over time, this effectively leads to quantum adiabatic computing systems, where quantum computing algorithms can be performed on the ground states [10]. For time-dependent Hamiltonians, both spin coupling and an external, time-varying field [11] or an output control signal [12] are present. It was argued that in time-varying spin systems, the problem of switch off can be mitigated, and the computation speed can be enhanced [13]. In general, an external

field can serve to increase the computational capacity even for relatively simple spin system structures [12,14]. However, it is challenging to analyze and realize time-dependent control of spin systems. Recently, the idea of embedding a time-dependent Hamiltonian into a time-independent one was studied, but the generality or universal applicability of this approach remains unknown [15,16]. In addition, deep neural-network-based techniques for quantum state classification and reconstruction have been proposed [17,18].

In recent years, the inverse problem of spin systems has attracted a great deal of attention. The basic question is, given only limited access to the system, i.e., when only part of the system can be measured, can the global structure of the spin system be determined? Previous efforts focused on monitoring the Hamiltonian as a function of time through the eigensystem realization algorithm (ERA) [19,20], compressive sensing [21,22], machine learning [15,16], or quantum quench [23]. The basic idea is to find the coefficients of the power series terms constituting the Hamiltonian in some basis. However, when applied to time-dependent quantum Hamiltonians, these approaches are limited to systems of a single spin or those with a special type of external field [22,24,25]. The general difficulty is that the functional form of the time signal generates an optimization problem in infinite dimensions [26], rendering inapplicable any optimization algorithm designed for finding a finite number of parameters. For the methods based on the eigenstates, difficulties arise when the system changes too fast with time [19,20,25]. Different inverse methods were tested using experimental data of time-independent spin systems [27]. A method of unsupervised learning based

*Ying-Cheng.Lai@asu.edu

on the principle of inheritance was proposed [28] to find the coupling profile and coefficients for spin systems. In addition, a method was proposed to find the local Hamiltonian from local measurements [25]. The previous studies focused on time-independent quantum Hamiltonian systems.

In this paper, we solve a general class of inverse problems in spin systems by exploiting machine learning [29]. Our work was partly inspired by the recent work on classical Hamiltonian neural networks (HNNs) [30–34], where the basic idea is to introduce a physics-based, customized loss function to “force” the dynamical evolution of the system to follow that stipulated by the classical Hamilton’s equations. However, the existing HNNs are not directly applicable to quantum Hamiltonians, thereby requiring new approaches. Our idea originates from the basic physical consideration that the dynamical evolution of spin systems is governed by the Heisenberg equations of motion. We are thus motivated to develop a class of Heisenberg neural networks (HENNs) by exploiting deep learning to predict the Hamiltonian but under the constraint of the Heisenberg equations of motion. The HENNs have the advantage of guaranteeing that the underlying quantum evolution possesses Hermitian structure. The quantum Hamiltonians to be studied in this paper are assumed to meet the following requirements: (i) they vary continuously with time (a commonly encountered situation in experiments), (ii) the measured spins are coupled with the rest of the spins directly or indirectly, and (iii) there are no Pauli terms in the Hamiltonian that commute with each other.

Our main results pertain to the original time-dependent quantum Hamiltonians, whose structure is to be determined based on incomplete local measurements, and the HENN, which is an artificial neural network for predicting the Hamiltonian of the original system. We treat the dynamical evolution of the original system in terms of both Schrödinger and Heisenberg pictures. We demonstrate that, with only local measurements, the local Hamiltonian can be recovered, similar to the solution of the local Hamiltonian learning problem [25]. In particular, defining the tomography fidelity as the ratio between the correctly predicted links and the total possible number of links in the underlying spin systems, we find that the fidelity can reach 90% even when the number of spins measured is much smaller than the system size. In fact, the predicted Hamiltonian contains global information about the coupling profile of the original quantum Hamiltonians. We note that the problem of network reconstruction or tomography has been well studied in classical nonlinear dynamical systems [35–39], and there was also a study of structure identification for time-independent quantum Hamiltonians [40]. Our work goes beyond the relevant literature in that we have successfully articulated and validated a general machine learning framework of quantum tomography for time-dependent quantum Hamiltonians.

Three remarks are in order.

Remark 1. It is worth noting that the problem of initialization in quantum Hamiltonian tomography is challenging and has not been solved. The current state of the field is that, even when measurement is done locally, initial state preparation for the whole system is still required. This is the case for algorithms such as the eigensystem realization algorithm

(ERA) [19,20]. Even for the problem of local Hamiltonian recovery, the requirement is that initially the system must be in an eigenstate [25]. To our knowledge, the only case in which initial state preparation is not required is when the spin system structure is already known [41]. The important feature of our work is a machine-learning approach to tomography of *time-dependent* quantum Hamiltonians without any prior knowledge about the network structure. As in the existing studies treating time-independent quantum Hamiltonians [15,16,19–22], a large number of given initial states is required. However, state preparation methods are currently available [42–44].

Remark 2. A closely related approach is quantum process tomography (QPT) [45,46], which has been investigated but for time-independent quantum Hamiltonian systems. When carrying out QPT, one prepares an initial quantum state, performs observations, and repeats the process for different initial states until the observations are sufficient for matrix inversion. The advantage of the QPT approach is that only local measurements are required. For a spin network of size n , the required number of observations is 16^n . There were experimental results for systems of two or three spins [47–49]. In comparison with QPT, our HENN approach thus has two advantages: applicability to time-dependent systems, and a significant reduction in time complexity from 16^n to 4^n .

Remark 3. Recently, a recurrent neural network (RNN)-based method was proposed to recover a time-independent or a time-dependent Hamiltonian from a single spin measurement in a spin system of up to seven spins [50]. There is a fundamental difference between our work and Ref. [50]. In particular, in Ref. [50], it is required that the coupling structure of the original Hamiltonian be pre-given, whereas our HENN method does not require the structure of the quantum Hamiltonian to be known *a priori*. In our work, the hidden structure of the Hamiltonian is first obtained through HENN, which can then be used to find the full Hamiltonian of the target system, e.g., by using the method in Ref. [50].

In Sec. II, we describe the HENN learning framework. In Sec. III, we test our machine-learning method using a variety of time-dependent quantum Hamiltonians, which include networks with short- or long-range interactions and two quantum gates. In Appendix A, we present analytic results with HENNs for one- and three-spin systems.

II. TIME-DEPENDENT QUANTUM HAMILTONIANS AND HEISENBERG NEURAL NETWORKS

Consider a system of spins coupled by an external field. The Hamiltonian is

$$H(t) = h^{(1)} + f(t)h^{(2)}, \quad (1)$$

where $h^{(1,2)}$ represent the time-independent Hamiltonian and $f(t)$ is a continuous function of time that is the result of the application of a time-dependent electrical or magnetic field. Suppose the system is initially in the state $|\psi_0\rangle$ at $t = 0$. In the Schrödinger picture where the state evolves with time but the operators are time-invariant, at time t the expectation value of an operator A is given by $\langle A \rangle_t$. In the Heisenberg picture where the state does not change with time but the operators

do, an operator evolves according to the Heisenberg equation

$$\frac{dA^H}{dt} = i[H^H(t), A^H(t)], \quad (2)$$

where the superscript H specifies that the corresponding matrix is in the Heisenberg picture, $H^H(t) = U_{t,0}^\dagger H(t) U_{t,0}$, and $U_{t,0}$ and $H(t)$ do not commute with each other due to the time dependence. Once $H^H(t)$ is known, the corresponding Hamiltonian in the Schrödinger picture $H(t)$ can be determined. The goal is to solve the Heisenberg equation based on the observations of A .

Since Eq. (2) is a set of linear equations in $H^H(t)$, for any time t the equations are solvable if the number of nonequivalent equations is no less than the number of unknown elements. That is, the noncommutative operators at all times, $A^H(t)$, are required to be known. This is a key difference from time-independent systems, where $H^H(t) = H$, so one operator at any time, $A^H(t)$, can be used as the noncommutative operator. In this case, once the observations (e.g., time series) are sufficient, the Hamiltonian can be fully determined [19,20].

The number of independent elements in the Hamiltonian matrix provides another angle to appreciate the complexity of the problem. In particular, for a system with n spins, at a specific time t , the Hamiltonian in Eq. (1) can be represented by a Hermitian matrix in terms of the $N = 2^n$ linearly independent states. There are altogether $N^2 = 4^n$ bases for an $N \times N$ Hamiltonian matrix that is Hermitian. To fully solve Eq. (2) will thus require all the 4^n measurements at a given time. For example, for a two-spin system, there are four linearly independent states, so in principle 16 observations are needed. These observations can be generated by the direct product of the Pauli matrices $S_{\alpha,\beta} = \sigma_\alpha^1 \otimes \sigma_\beta^2$, where α and β are integers ranging from 0 to 3, which correspond to the identity and the three Pauli matrices $\sigma_x, \sigma_y, \sigma_z$. For these 16 matrices, one is an identity that commutes with all other matrices. Consequently, we need at least $2^N - 1 = 4^n - 1$ measurements to fully determine the Hamiltonian.

When the quantum states of all spins can be measured, it is straightforward to obtain the Hamiltonian matrix through Eq. (2). A difficult situation is that only a small fraction of the spins in the network, e.g., one or two, can be measured. Experimentally, measurements or observations have been reported for one-, two-, and three-spin systems [51–53]. The pertinent question is, what can we learn about the whole network system when only local measurements in some subspace of the full space are available? To address this question, we decompose the Hamiltonian as

$$H = \underbrace{H_o + H_i}_{H_o'} + H_h, \quad (3)$$

where H_o is the subspace Hamiltonian for the observed spins, H_i represents the interaction between the observed and the nonobservable spins, and H_h is the Hamiltonian for the nonobservable spins. Let $H_o' \equiv H_o + H_i$, which is the subspace Hamiltonian that contains information directly related to the observed spins.

Take a three-spin system as an example, as shown in Fig. 1(a). The three spins are labeled with 1,2,3, and we assume that only the first spin can be measured. The subspace of

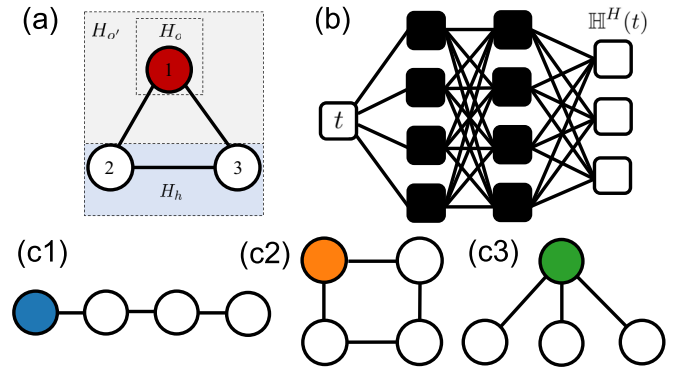


FIG. 1. Three- and four-spin systems and the machine-learning architecture. (a) Schematic illustration of the local observation of the Hamiltonian in a three-spin system. Say only one node or spin (spin no. 1) can be observed, which corresponds to the Hamiltonian H_o . The Hamiltonian for the nonobservable nodes and their interactions are labeled as H_h . (b) Machine-learning (neural network) architecture, where the nodes in the hidden layers are represented by black squares, the input and output are denoted by open squares, and the various weighted links (solid line segments) connect the input to the output. The input is one-dimensional: it is simply the time variable t . The output constitutes the elements of the matrix $\mathbb{H}^H(t)$ whose size is determined by the size of the spin system. The weight associated with each link is calculated by the autograd method to minimize the custom loss Eq. (4). (c1)–(c3) Possible architectures of a four-spin system, where the filled circle represents the observable spin in the network. The networks in (c1)–(c3) have a chain, a cyclic, and a tree structure, respectively. For $n = 3$ and 5, structures similar to those in (c1)–(c3) exist.

H_o contains three bases corresponding to the Pauli matrices for the first spin $H_o = \sigma^1$, and H_i contains two-body interactions between the first spin and the second or the third spin and the three-body interaction:

$$H_i = \sigma^1(\sigma^2 + \sigma^3 + \sigma^2\sigma^3).$$

The subspace Hamiltonian H_h contains the Pauli matrices for the second and third spins as well as the two-body interaction between them: $H_h = \sigma^2 + \sigma^3 + \sigma^2\sigma^3$. Overall, this is a three-node spin system, where the nodal interactions represent different links. For each node, three independent quantities (the three Pauli matrices) are needed to characterize the spin polarization, which generate different combinations of coupling. A unique feature of spin systems, which is not present in classical complex networks, is that one link can couple more than two nodes.

The decomposition scheme in (3) is valid only in the Schrödinger picture. In the Heisenberg picture, different subspaces are mixed together in the time evolution, so all the subspace must be simultaneously determined. For limited observations, the solutions of the Heisenberg equation can be nonunique. To overcome this difficulty, we exploit machine learning to predict the Hamiltonian. Inspired by the work of HNN, whose loss function is based on the Hamilton's equations of motion [30–34] for time-independent spin systems, we articulate a general class of HENNs that conform with the Heisenberg equations of motion with broad applicability to both time-dependent and time-independent spin systems.

TABLE I. Training parameters for HENN.

Description	Values
Number of initial states for $n = 3, 4, 5$	100, 300, 1100
Number of observations for one or two spins	3, 15
Number of discrete-time points	100

Figure 1(b) shows our neural network architecture with two hidden layers. The input is one-dimensional: it is simply the time t . Each layer is a convolution of the preceding layer: $\mathbf{a}_l = \tau(\mathcal{W}_l \cdot \mathbf{a}_{l-1} + \mathbf{b}_l)$, where \mathbf{a}_l is the state vector of the l th layer, \mathcal{W}_l is the weighted matrix connecting layers l and $l-1$, \mathbf{b}_l is the bias vector of layer l , and τ is a nonlinear activation function, e.g., $\tau = \tanh$. The matrix \mathcal{W} and the bias vector \mathbf{b}_l are to be determined through training based on spin measurements. The output is the Hamiltonian matrix in the Heisenberg picture. In our study, we use two hidden layers, each with 200 nodes. The neural network is built by TENSORFLOW and the KERAS package [54]. We use the stochastic gradient descent (SGD) and adaptive momentum (Adam) methods to determine the optimal weighted matrix \mathcal{W}_l and the bias vector \mathbf{b}_l by minimizing an appropriate loss function [55]. In particular, we define our loss function as the mean-square error in the time derivatives of the observation as

$$\mathcal{L} = \sum_{\text{observations}} |\langle \dot{A}(t) \rangle_{\text{real}} - \langle \dot{A}(t) \rangle_{\text{pred}}|^2, \quad (4)$$

where $\dot{A}_{\text{pred}}(t) = i[H^H(t), A(t)]$, and the matrix $H^H(t)$ is the output of the HENN. Once the time derivatives for some given observations are known, we input them to the loss function as the target to train the HENN and subsequently to predict the Hamiltonian. Due to incomplete measurement and finite optimization steps, the predicted Hamiltonian varies over different rounds of training. It is thus necessary to take the statistical average of the prediction and to calculate the variance.

The training data are measured time series, from which the corresponding derivative of the loss function can be estimated. The total amount of training data depends on three factors: the number of linearly independent states, the number of observations, and the number of time discrete points. In Table I, we list the amount of training data required for different examples. For example, for a chain structure of $n = 4$ spins with one spin observed, the required number of training data points is $300 \times 3 \times 100 = 90\,000$. Since the HENN is trained for a specific structure, for a different Hamiltonian the deep neural network needs to be retrained.

It can be shown that the sub-Hamiltonian H_σ in Eq. (3) containing information directly related to the observed spins can be recovered [25]. For the subsystem not directly related to the observed spin, its Hamiltonian H_h cannot be fully recovered. However, we can show that, in the subspace of H_h , if the machine-predicted coupling value between two nodes is smaller than some threshold, then it effectively indicates null coupling. This means that our HENN is capable of determining the coupling configuration for the quantum Hamiltonian based on whether the predicted Hamiltonian matrix elements are zero or finite, providing a solution to the tomography problem for the whole system. In particular, the tomography

contains two types of information: whether the spins are coupled, and if so, how they are coupled. The first one is related to the spatial structure of the network, as exemplified in Fig. 1(a), where spin 1 is coupled to spins 2 and 3. The second type of information gives the type of coupling among all possible coupling configurations determined by the spin polarization vector at each node.

The prediction phase of our HENN thus consists of the following steps:

First, for a given quantum spin system, we take measurement A from some part of the system and calculate the corresponding matrix elements $\mathbb{A}^H(t)$ based on the linear equation

$$\langle \psi_0 | A^H(t) | \psi_0 \rangle = \langle A \rangle_t.$$

To obtain the matrix elements, the number of linearly independent initial states must be larger than the number of independent elements of the matrix. Specifically, for a spin system with n spins, at least 4^n linearly independent initial states are needed.

Second, we build up a neural network as in Fig. 1(b) with input time t and output as the matrix elements $\mathbb{H}^H(t)$. We train the network using the loss function defined in Eq. (4). After the HENN is properly trained, we evaluate the Hamiltonian for a given time series, and we convert it into the Schrödinger picture. The coupling among the nodes can be obtained from the decomposition

$$\begin{aligned} \mathbb{H}(t) &= c_0(t)\mathbb{I} + \sum_{i,j} c_{ij}(t)\sigma_j^i, \\ &+ \sum_{i,j,k,m} c_{ijkm}(t)\sigma_j^i\sigma_m^k + \dots \equiv \sum_i c_i(t)S_i, \end{aligned} \quad (5)$$

where S_i is the basis of the N -dimensional Hamiltonian matrix, and $c_i(t)$ is the corresponding coupling coefficients at time t . We choose S_i to be the direct product of the Pauli matrices plus the identity matrix. The coefficients $c_i(t)$ determine the coupling configuration of the system.

Third, after obtaining the time series of the coupling coefficients, we take the time average for each basis $\bar{c}_i = \int_0^t |c_i(t)| dt$ and normalize them by their maximum value. We set some threshold: any value above which an existent coupling is indicated between the corresponding spins.

To better illustrate our HENN-based machine-learning procedure, in Appendix A we present two explicit examples for a HENN-predicted Hamiltonian: a one-spin system and a three-spin system.

III. RESULTS

We test the predictive power of the proposed HENNs for a number of spin systems. As noted, in a quantum spin system the concept of links can be quite different from those in classical networks. In particular, one link is referred to as a specific way of coupling in the underlying spin system. For a system with n spins, the total number of linearly independent states is 2^n . The total number of independent elements in the Hamiltonian matrix is 4^n , which is the total number of possible ways of coupling in the system. The links are generated by the direct products of the Pauli and identity matrices. The types of links

include self-coupling, two-body interactions, and long-range interactions. A quantity to characterize the machine-learning performance is the tomography fidelity, defined as the ratio between the number of correctly predicted links and the total possible number of links. Disregarding the identity matrix, we define the tomography fidelity as

$$F_t = \frac{4^n - 1 - (\text{no. of missing links})}{4^n - 1}, \quad (6)$$

where the tomography is meaningful for $F_t > 50\%$. A more useful characterizing quantity is the success in identifying the structure of H_h , as this is proof that the method can not only yield the structure of the subsystem from which measurements are taken ($H_{o'}$), but also information about the complementary subsystem from which no observations are made (H_h), so that information about the whole system can be obtained. This alternative fidelity measure is defined as

$$F_{t'} = \frac{4^{n'} - 1 - (\text{no. of missing links})}{4^{n'} - 1}, \quad (7)$$

where $n' = n - n_{\text{obs}}$, and n_{obs} is the number of spins from which observations are taken.

Another quantity is the fidelity measure for local Hamiltonian $F_{o'}$ defined as

$$F_{o'} = 1 - \frac{\|H_{o'}^{(\text{pred})} - H_{o'}^{(\text{real})}\|}{\|H_{o'}^{(\text{real})}\|}, \quad (8)$$

where $H_{o'}^{(\text{real})}$ and $H_{o'}^{(\text{pred})}$ are the real and predicted local Hamiltonians, respectively.

A. Tomography of spin systems based on two-body interactions

The sub-Hamiltonians $h^{(1)}$ and $h^{(2)}$ in (1) of a spin system with two-body interactions are given by

$$h^{(1,2)} = \sum_{i=1}^n \sum_{j=1}^3 c_{ij}^{(1,2)} \sigma_j^i + \sum_{i=1}^n \sum_{j=i+1}^n \sum_{m=1}^3 \sum_{l=1}^3 w_{ij} c_{ijml}^{(1,2)} \sigma_m^i \sigma_l^j, \quad (9)$$

where c 's are random numbers between 0 and 1. The superscript of σ indicates the number of spins, which varies from 1 to n , the subscripts 1,2,3 denote the x , y , and z components of the spin, respectively, w_{ij} is the ij th element of the adjacency matrix as in a conventional, undirected network, where $w_{ij} = 1$ indicates there is coupling between spin i and spin j , otherwise $w_{ij} = 0$. The first term of h contains self-couplings, and the second term contains two-body couplings. Due to the exponential growth of the computational overload with the number of spins in the network, we limit our study to networks with $n \leq 5$ spins. The Hamiltonian (9) arises in a variety of physical situations such as the Heisenberg model or spin glass systems [56,57]. The time dependence in the general Hamiltonian (1) is introduced into the network with the following ‘‘driving’’ function of time:

$$f(t) = \sin(\omega t + 2\pi\phi), \quad (10)$$

where ω and ϕ are random numbers whose values are taken between 0 and 1.

We test HENNs with the three structures shown in Figs. 1(a) and 1(c1)–1(c3). The main difference among them lies in the degree of the observed node. For example, for the networks in Figs. 1(c1)–1(c3), the degree of the observed spin is 9, 18, and 27, respectively. To generate the data, we choose 100, 300, and 1100 random initial conditions for $n = 3, 4$, and 5. For each initial condition, we numerically integrate the Heisenberg equation (2) for $0 < t < 5$, and we extract from this time interval 100 equally spaced points as the measurement data. The calculated time series for a given initial state correspond to observations of σ_x , σ_y , and σ_z for the specific local spin in the network from which measurements are taken. We take the time derivative defined in Eq. (4) as the loss function for training the HENN. Following the steps described in Sec. II, we obtain the predicted interaction structure of the network. Comparing with the actual structure gives the tomography fidelity. Since the fidelity may vary for a different Hamiltonian, for each specific type of networks, we repeat this process 100 times.

Figure 2(a) shows the results of reconstructing the cyclic network of three spins in Fig. 1(a), where the degree of each node is 18 (excluding self-interactions) and there are 64 distinct links in the network. What is displayed is the average predicted coupling value \bar{c} versus the link index, and the blue squares and red circles denote the existent and null links, respectively. The dashed horizontal line defined at 10% of the maximum coupling value can separate the majority of the existent links from the majority of the null links. Figures 2(b) and 2(c) show the results from similar cyclic networks but with four and five spins, respectively, with the same legends as those in Fig. 2(a). These results indicate that, even when measurements are taken from only one spin, the coupling structure of the time-dependent Hamiltonian can be predicted by our HENN with a reasonably high accuracy.

A heuristic reason that the HENN is able to predict the structure of the spin system correctly from only local measurements is as follows. Recall that the input to the HENN is time, a continuous variable. The differential property of the neural network guarantees that the predicted Hamiltonian must be continuous and the time change for the predicted Hamiltonian must follow the Heisenberg equation as stipulated by the physically meaningful loss function. With these constraints, data from different time will instill the correct physical relationships among the dynamical variables into the neural network. As a result, the difficulty of the nonuniqueness of the solutions when solving the linear equations is overcome.

To further characterize the performance of HENNs for different network structures, we calculate the average fidelity measures for nine distinct networks that include the chain, cyclic, and tree structures in Figs. 1(c1)–1(c3), respectively, each with $n = 3, 4$, and 5 spins, as shown in Figs. 3(a), 3(b), and 3(c) for the measures F_t , $F_{t'}$, and $F_{o'}$, respectively. For the network structures in Figs. 1(c1)–1(c3), the degrees of the measurement spin are 9, 18, and 27, respectively. For a fixed number of spins in the network, the fidelity value decreases with the degree of the measurement spin.

The results in Fig. 3 can be explained as follows. In general, a higher degree of the observed spins means that the measured time series are more complicated. Our calculation shows that the accuracy for the predicted Hamiltonian directly

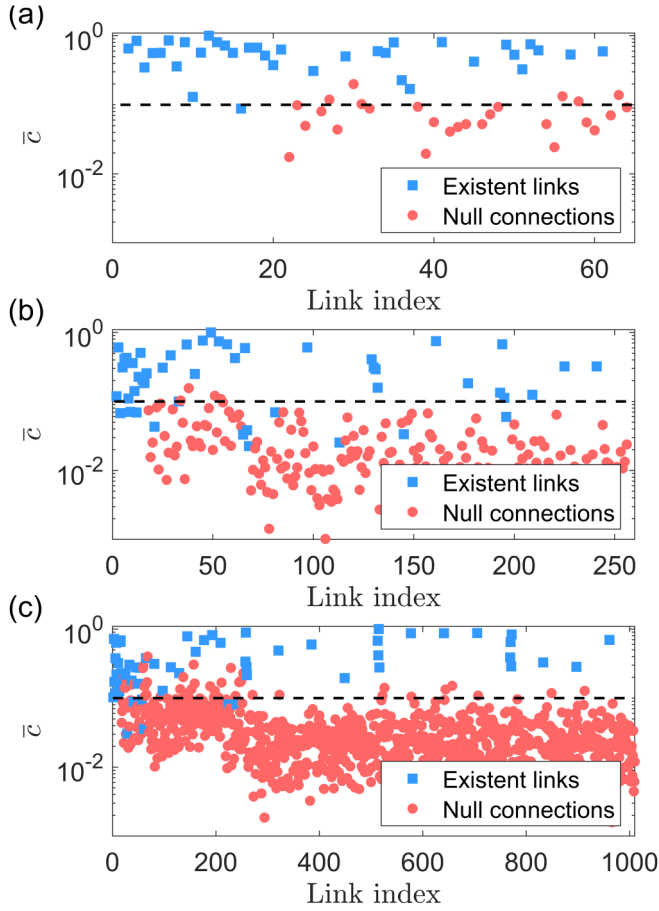


FIG. 2. Tomography performance of HENN for cyclic networks of $n = 3, 4$, and 5 spins. The network structure is given in Fig. 1(a). (a) Reconstructed coupling value \bar{c} vs the total number of possible links. The result is for one of the spin systems with the average tomography fidelity value from 100 random realizations. The abscissa represent the number of possible links for $n = 3$, where the basis ranges from $\sigma_0^1 \otimes \sigma_0^2 \otimes \sigma_1^3$ to $\sigma_3^1 \otimes \sigma_3^2 \otimes \sigma_3^3$, where the total number of possible links is $4^n - 1 = 63$ (with the identity matrix taken away). The blue squares represent the true, existent links, while nonexistent or null links are denoted by red circles. The horizontal dashed line is taken at 10% of the predicted maximum coupling value. (b,c) Results from $n = 4$ and 5 , respectively, with the same legends. In all cases, the horizontal dashed line can serve as a threshold for separating the majority of the existent links from the majority of the null links, attesting to the ability of the machine-learning scheme to infer the whole network structure from local measurements only.

connected to the observed node F_{σ} remains approximately the same, but the prediction accuracy of the hidden structure decreases with the degree of the observed spin. Note that, for $n = 3$, a cyclic structure and a tree structure have the same degree. For the tree structure, the HENN reveals a coupling between two nonobserved nodes that does not exist in the original system. This is the reason that the tomography fidelity is smaller for the tree structure than that for the cyclic structure.

Note that the measure F_t is defined for the whole network, which takes into account not only the links between the measurement spin and the nonobservable spins, but also

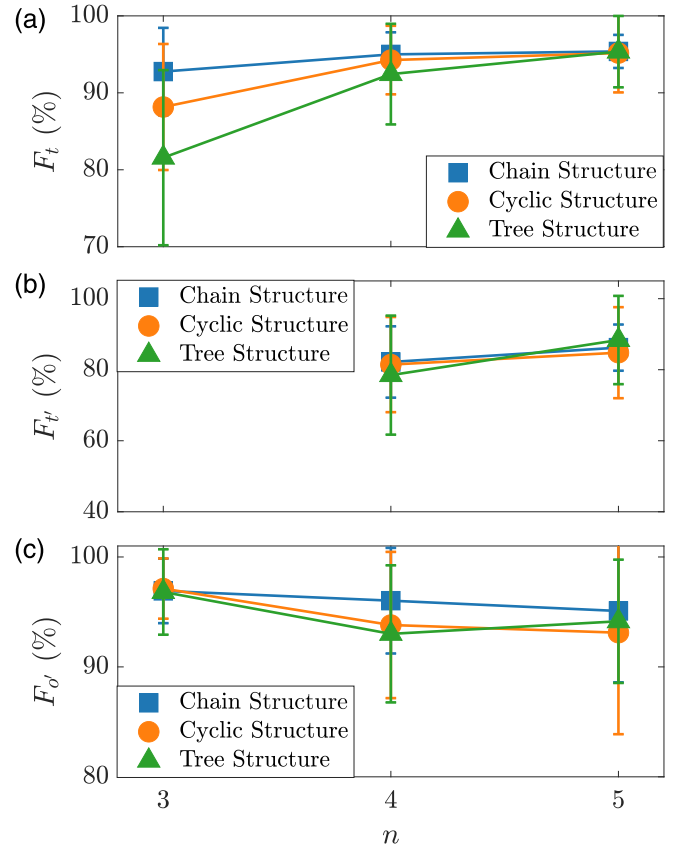


FIG. 3. Tomography fidelity measure. (a) Average tomography fidelity F_t and the standard deviation for nine distinct networks of three types of structures in Figs. 1(c1)–1(c3), respectively, each with $n = 3, 4$, and 5 spins. In all cases, local measurements from only one spin are taken. (b) Average alternative tomography fidelity $F_{t'}$ for $n = 4$ and 5 , corresponding to $n' = 3$ and 4 , respectively. (The results from $n = 3$ contain large statistical errors because of the relatively small size of the system, and thus they are not shown so that the results for $n = 4$ and 5 can be seen clearly.) In all cases, the fidelity values are above 80%, indicating the predictive power of HENN. (c) The accuracy for the sub-Hamiltonian that contains information directly related to the observed spins H_{σ} for $n = 3, 4$, and 5 spins with 48, 192, and 768 time series, respectively.

the links among the nonobservable spins, where the latter are characterized by the alternative tomography fidelity measure $F_{t'}$. Since this measure is purely for the nonobservable spins from which no measurements are taken, we expect its value to be lower than that of F_t , as shown in Fig. 3(b). In spite of the reduction in comparison with F_t , the values of $F_{t'}$ for $n = 4$ and 5 are still relatively high: approximately 80% and larger, attesting to the power of our HENN scheme to extract information from the nonobservable spins.

The accuracy for the predicted Hamiltonians directly related to the observed spin is shown in Fig. 3(c). Take a four-spin system as an example. There are three self-coupling terms: 27 two-body interactions, 81 three-body interactions, and 81 four-body interactions. For comparison, we use 192 time series. As shown in Fig. 3(c) for different structures and different numbers of spins, the values of F_{σ} are larger than 90%. For spin systems with a tree structure, the fidelity is

TABLE II. Tomography fidelity measures under different driving functions.

	$f(t) = t/5$	$f(t) = \sin(\frac{\pi}{5}t)$	$f(t) = \exp[-(t - 2.5)^2]$
F_t	97.4% \pm 1.7%	96.7% \pm 1.7%	96.3% \pm 2.4%
$F_{t'}$	90.7% \pm 6.4%	88.3% \pm 6.5%	87.9% \pm 7.3%
$F_{d'}$	98.0% \pm 1.0%	96.6% \pm 1.3%	95.5% \pm 1.9%

slightly lower than that for the other two structures. As the system size increases, the variance becomes larger. However, the overall fidelity values are uniformly high.

Another issue is the effects of the type of driving functions on the tomography fidelity. To be illustrative, we choose three different driving functions: $f(t) = t/5$, $f(t) = \sin(\pi t/5)$, and $f(t) = \exp[-(t - 2.5)^2]$ for $t \in [0, 5]$, representing linear, sinusoidal, and Gaussian pulse behaviors, respectively. Using the cyclic structure of four spins with measurement obtained from one spin as shown in Fig. 1(c2), we calculate the fidelity measures F_t , $F_{t'}$, and $F_{d'}$ and list the results in Table II. These results indicate that the fidelity is generally higher for the relatively simple driving function $f(t) = t/5$. In Table II, the sinusoidal driving and Gaussian pulse contain one period. For random frequency ω between 0 and 1, and for two oscillation periods, the accuracy decreases slightly, indicating that for more complex time series containing multiple oscillations, the error will increase. Also, in our setting, the time series start from $t = 0$, since the Hamiltonian to be predicted is in the Heisenberg picture. However, to obtain the coupling profile of the spin system, we need to change the Hamiltonian into the Schrödinger picture, a task that will become difficult if an initial period of the time series is missing.

Utilizing two-body coupling spin systems to evaluate the performance of the HENNs has certain limitations. In particular, for a given network structure, when the number of spins increases, the error appears to decrease, due mostly to the exponential growth in the total possible number of links in the network, which is an artifact. In some cases, the prediction results can be trivial as the system size increases. For example, if all the two-body couplings are null, then for $n = 3$ the tomography fidelity value will be about 40% because approximately 60% of the links are of the two-body type. Similarly, for $n = 4$ and 5, approximately 20% and 5% of the links are of the two-body type, leading to artificial fidelity values of about 80% and 95%, respectively. Comparing with the results in Fig. 3, for $n = 3$ and 4, the trivial prediction gives lower fidelity values, but the difference diminishes for $n = 5$. Consequently, based solely on two-body interactions, the fact that the tomography fidelity increases with the system size is not synonymous with a better performance of the algorithm for larger systems. For accurate tomography of quantum spin systems, long-range interactions must be included.

B. Tomography of quantum spin systems with long-range interactions

We consider the more general Hamiltonian that contains all short- and long-range interactions. Physical applications in-

clude the development of quantum gates such as the Toffoli or the Fredkin gate that requires three-body interaction [58], spin glass with infinite-range interactions [57], and quantum computing that requires high coherence [53,59]. We decompose the Hamiltonian into two components, $h^{(1,2)}$, as in Eq. (1), which are given by

$$h^{(1,2)} = \sum_{i_1, i_2, \dots, i_n=0}^3 r c_{i_1 i_2 \dots i_n}^{(1,2)} \sigma_{i_1}^1 \sigma_{i_2}^2 \dots \sigma_{i_n}^n, \quad (11)$$

where $c_{i_1 i_2 \dots i_n}^{(1,2)}$ are random numbers between 0 and 1, and r takes on the values of 1 or 0 with equal probabilities. The network comes into existence only for $r = 1$. The function $f(t)$ rendering the system time-dependent is chosen according to Eq. (10).

We consider systems with $n = 3, 4$, or 5 spins with 100, 300, and 1100 random initial conditions, respectively. Observing one spin leads to time series of σ_x , σ_y , and σ_z from this spin. If two spins can be measured, we choose the observation variable to be $\sigma_\alpha^1 \otimes \sigma_\beta^2$, where α and β are integers from 0 to 3, corresponding to the identity and the three Pauli matrices, respectively. Excluding the identity operation, we have 15 measured time series of 100 equally spacing points in the time interval $0 < t < 5$.

Following the procedure described in Sec. II, we train the HENN to predict the coupling configurations of the spin systems with long-range interactions. Unlike the case in which only two-body interactions are taken into account, here the links are chosen randomly: we consider all possible links, and any specific link does or does not exist with equal probabilities. Figure 4 shows the prediction performance for a network of $n = 4$ spins, where panels (a) and (b) correspond to the cases of measuring one and two spins, respectively. When only one spin is measured [Fig. 4(a)], most of the existent and nonexistent links can be distinguished by the 10% threshold line, yet there are still quite a few links that are on the “wrong” side. When two spins are measured, the prediction accuracy is higher as there are far fewer incorrectly predicted links. This is intuitively reasonable, as measuring more spins is equivalent to imposing more constraints on the predicted Hamiltonian so as to improve the prediction accuracy.

Figure 5 shows the fidelity measure of predicting random networks of $n = 3, 4$, and 5 spins from observing one spin or two spins. As shown in Fig. 5(a), the fidelity value decreases as the number of spins increases. This is expected because, when observing a fixed number of spins, a larger system means more nonobservable spins and leads to larger prediction uncertainties. Another expected feature is that, for a fixed system size, observing two spins leads to higher fidelity values [about 95% in Fig. 5(a)] as compared with the case of observing one spin [about 85% in Fig. 5(a)]. Figure 5(b) shows that the fidelity measure with respect to the hidden structure exceeds 50%, indicating that the interactions among the nonobservable spins can be predicted with statistical confidence. In fact, as stipulated by Eq. (11), our HENN can predict not only the existence of the interactions, but also their strength as characterized by the coefficients $c_{i_1 i_2 \dots i_n}^{(1,2)}$.

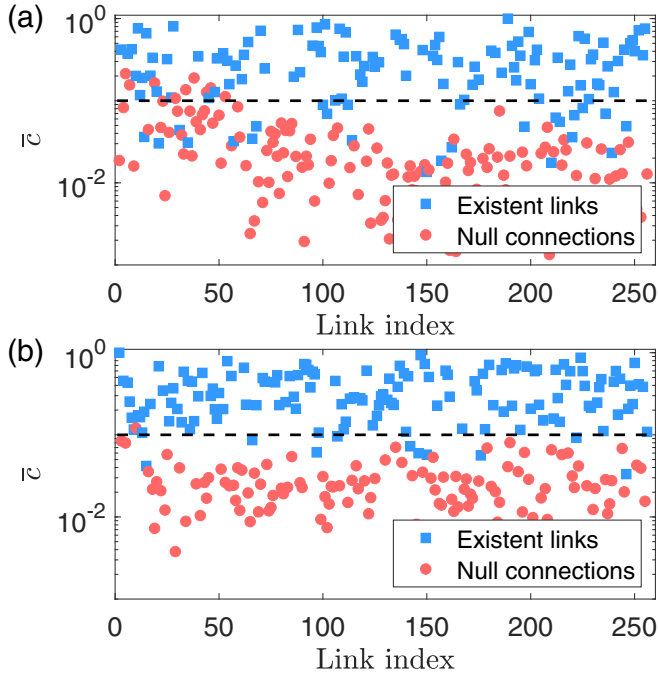


FIG. 4. Prediction performance of HENN for a network of four spins with long-range interactions. (a) Reconstructed coupling coefficients vs those based on time series measured from one spin only. The results are from one realization of the spin system with the fidelity value equal to the average fidelity value over 100 random realizations. The legends are the same as those in Fig. 2. (b) The corresponding results when two spins are observed with the time series as described in the text.

C. Tomography of quantum gates

We apply our HENN framework to a class of systems that are fundamental to quantum computing: quantum logic gates. Such a gate typically consists of two or three coupled spins [1]. To be concrete, we consider the Toffoli and Fredkin gates with three spins [58], and we demonstrate that HENN can perform the tomography. Experimentally, these quantum logic gates can be implemented with optical devices [60,61] or superconducting qubits [62].

The Toffoli gate is a Control-Control Not gate, i.e., when the first and second spins have the signal $|11\rangle$, the third spin will flip [58], which requires a certain time, e.g., $t = 1$. By this time, the evolution operator is

$$U_{\text{Toffoli}} = \begin{pmatrix} \mathbb{I}_6 & \\ & \mathbb{X}(t=1) \end{pmatrix}, \quad (12)$$

where \mathbb{I}_6 is the 6×6 identity matrix,

$$\mathbb{X}(t=1) = \begin{pmatrix} 0 & 1 \\ 1 & 0 \end{pmatrix} \quad (13)$$

flips the third spin, and the off-diagonal blocks are zero. Similarly, the time evolution operator for the Fredkin gate is

$$U_{\text{Fredkin}} = \begin{pmatrix} \mathbb{I}_5 & & \\ & \mathbb{X}(t=1) & \\ & & 1 \end{pmatrix}. \quad (14)$$

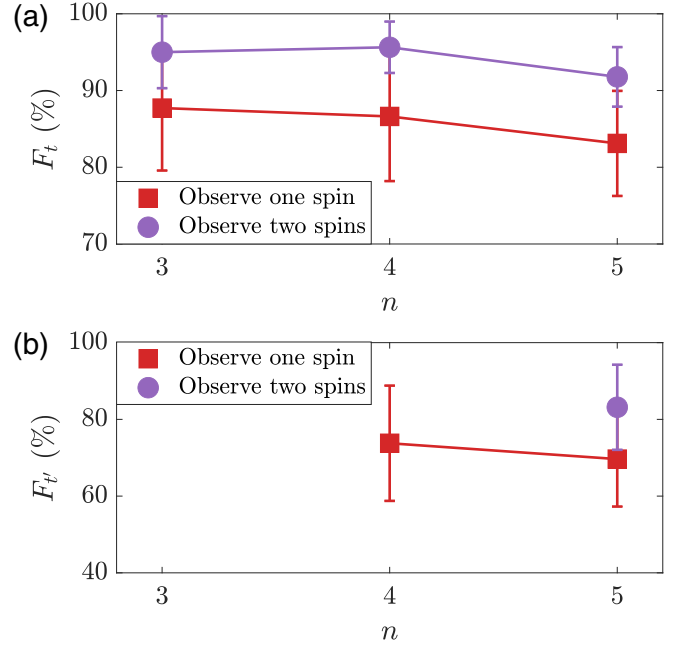


FIG. 5. Fidelity of predicting random spin systems from observing one spin or two spins. (a) Average tomography fidelity F_t and the standard deviation. Each data point is the result of averaging over 100 random initial-condition realizations. (b) The corresponding results for F_t' . In the case of observing one spin, results for $n = 3$ contain large fluctuations. When two spins are observed, only the five-spin system generates reasonable values of F_t' . In general, observing two spins leads to higher fidelity values.

A physical constraint for $\mathbb{X}(t)$ is that, at $t = 0$, the system does not evolve, so $\mathbb{X}(t=0) = \mathbb{I}_2$. To build such a time evolution operator, one can use the underlying time-independent Hamiltonian as a base (Appendix B), where the elements of $\mathbb{X}(t)$ are periodic functions, with the fundamental frequency as the flipping rate. Searching for possible forms of $\mathbb{X}(t)$ is a basic issue in designing quantum logic gates [15,16].

To demonstrate the applicability of HENN to quantum logic gates in a concrete manner, we choose $\mathbb{X}(t)$ as

$$\mathbb{X}(t) = \frac{1}{2} \begin{pmatrix} 1 + \exp(i\pi t) & 1 - \exp(3i\pi t) \\ 1 - \exp(3i\pi t) & 1 + \exp(i\pi t) \end{pmatrix} \quad (15)$$

to generate the time-dependent Hamiltonian. For training, we generate time series from $t = 0$ to 1 with the time step $dt = 0.01$ from 100 random initial conditions, and the time evolution of the dynamical variables of the third spin is taken as the measurements. For comparison, we calculate the tomography fidelity for both the time-dependent and the corresponding time-independent systems.

Table III lists the values of the tomography fidelity for both Toffoli and Fredkin gates. It can be seen that the average

TABLE III. Tomography fidelity for Toffoli and Fredkin gates.

	Toffoli gate	Fredkin gate
Time-dependent	81% \pm 3%	87% \pm 3%
Time-independent	85% \pm 4%	92% \pm 3%

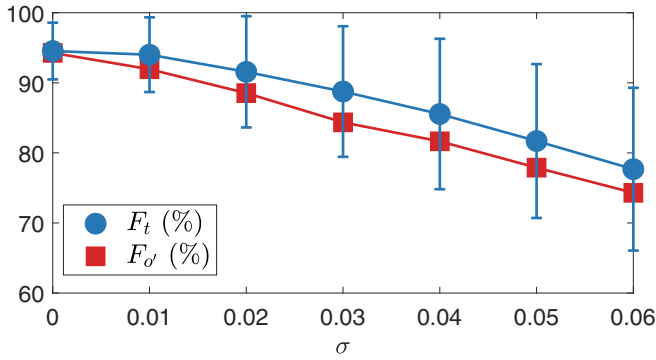


FIG. 6. Network tomography fidelity under Gaussian noise. The system is a cyclic network of four spins constructed according to Eq. (9), where measurements are taken from one node. The additive white Gaussian noise has the variance $\sigma = 0.06$, which is approximately one-third of the average variation of the measured time series. The two sets of data represent the two fidelity measures F_t and F_d vs the noise amplitude, where F_d characterizes the difference between the recovered local Hamiltonian and the true one.

tomography fidelity for the Fredkin gate is larger than that for the Toffoli gate. Both gates have seven links, but the Fredkin gate has more three-body coupling terms than the Toffoli gate. This means that, for the Fredkin gate, more links are directly connected to the observed spin. When the system becomes time-independent, the fidelity values are slightly higher.

D. Quantum tomography under noise

Noise arising from random coupling with the environment will impact the quality of quantum tomography. Previously, the issue of noise was studied in the context of Hamiltonian learning [19,25]. Here, we study the effect of noise on our HENN-based quantum tomography. A relevant point is that HENN can predict the correct form but only of the local Hamiltonian, so the Hamiltonian for the whole spin system cannot be uniquely determined. This is similar to obtaining the local Hamiltonian from local observations [25].

As a concrete example, we study a cyclic network of four spins, where measurements are taken from only one spin, which are subject to additive white Gaussian noise. The local Hamiltonian H_o constitutes the three Pauli matrices for the observed spin, giving rise to three measured time series. The Hamiltonian H_o consists of the three Pauli matrices for the observed spin and all the interactions that involve the observed spin. In particular, there are 27 two-body interactions, 81 three-body interactions, and 81 four-body interactions. As a result, H_o can generate a total of 192 time series. From a different perspective, for a four-spin system, the total number of dynamical variables is 256. When we measure one spin so that the other three spins are not observed, H_h contains one-fourth of the dynamical variables (4^3) while H_o has the remaining variables.

Figure 6 shows that the fidelity value decreases, albeit slowly, as the noise amplitude increases. The robustness of HENN against weak noise is rooted in the goal of HENN: finding one Hamiltonian that minimizes the loss function. However, for strong noise, the derivatives in the Heisenberg

equation will generate unstable solutions. Figure 6 also reveals the similarity between local Hamiltonian recovery and the tomography of the whole system. In particular, it demonstrates that HENN can recover not only the local Hamiltonian, but also the hidden structure of the spin system, which is not a simple extension of the local Hamiltonian.

IV. DISCUSSION

In quantum tomography, learning time-dependent systems from partial and limited measurements remains a challenge, as it requires optimization in an infinite-dimensional space. Machine learning provides a potentially viable solution. Because of the underlying physics of the spin systems, it is necessary to incorporate the physical constraints into the learning algorithms. Historically, the idea of developing physics-informed artificial neural networks was conceived almost three decades ago [30], but it has recently attracted revived attention, particularly in the context of Hamiltonian neural networks (HNNs) [31–34]. Our idea is that, for time-dependent quantum systems, the Heisenberg representation is natural in which the operators evolve with time as governed by the Heisenberg equation. Neural networks taking into account the physical constraints manifested as the Heisenberg equation should provide an approach to tomography of time-dependent quantum systems. Using spin systems that have been exploited extensively in quantum computing as a paradigm, we have developed a class of Heisenberg neural networks (HENNs) and demonstrated that, based on the time series measurements of local spin variables, not only the local Hamiltonian but that of the whole spin system can be faithfully determined. The method is effective even when measurements are conducted on a small part of the system, e.g., measuring one spin in a five-spin system. Considering that the existing algorithms on quantum tomography of spin systems were designed for networks whose structures are completely known [41,63,64], our work represents a useful complement.

For quantum tomography of time-dependent interacting spin systems, we have tested a variety of network structures. In general, the tomography fidelity depends on the interacting structure of the network. For example, it is inversely proportional to the degree of the spin from which measurements are taken (Fig. 3) when the spin system is relatively dense, as a large degree means more interactions with the nonobservable spins. The fidelity value also depends on the number of observed spins relative to the total number of spins in the network, where, naturally, measuring more spins can lead to higher fidelity values (e.g., Fig. 5). Indeed, a comparison of the tomography results from the Toffoli gate with those from the Fredkin gate reveals explicitly that more coupling links with the spin being measured lead to increased fidelity values when the spin system is relatively sparse.

A number of factors can affect the tomography accuracy. For the spin systems studied, the choices of the coupling and the time dependence as characterized by the driving function $f(t)$ are arbitrary. Our study has revealed that the tomography quality does not depend on the time signal insofar as the length of the measured time series is proper, but the HENN predicted Hamiltonian tends to deviate from the true one after approximately half of the driving period. If the time series

are too short, e.g., a fraction of the driving period, or if the time series are too long, e.g., more than a few driving periods, the resulting fidelity value would decrease. Another factor that can affect the fidelity is heterogeneity in the couplings in the network. For the results in this paper, the distribution of the couplings in the spin system is assumed to be uniform, where the typical fidelity value achieved is about 90%. However, we find that large variations in the coupling strengths can make the HENN ineffective. The ratio between self- and mutual couplings can also affect the tomography, where if the former dominate the latter, the errors in the tomography can be reduced.

Possible extensions of this work are as follows. When implementing the HENN, the initial states must be specified subject to a number of constraints. That is, it is necessary to know the initial quantum state of each spin. For time-independent systems, quantum tomography of spin networks is possible even if the initial states are not completely specified [41] or if the dimension of the system with a given coupling structure needs to be determined [65,66]. However, to our knowledge such methods are applicable to time-independent systems only. For example, in Ref. [41], a time-independent Hamiltonian with a specified structure was reconstructed. Since the structure is known *a priori*, the matrix representation of the observables can be expanded to have a few unknown parameters. For sufficiently long time series, the original Hamiltonian can be constructed. At present, quantum tomography of time-dependent systems with partial initial conditions or incomplete information about the system is an open problem.

The second issue is scalability. For a spin system of size n , HENN requires 4^n measurements. Calculating the matrix representation of the observable $A(t)$ can thus be time-consuming for large systems. In the prediction phase, another potential issue could arise: the predicted Hamiltonian can contain many terms, requiring the neural network to be extraordinarily large. Recently, neural networks with more than 100 billions parameters have been constructed [67], with applications to large systems with 100 spins [25]. The scalability of our HENN algorithm to large time-dependent spin systems is an important open issue worth further investigation.

The third issue concerns the effects of noise. In the study of noisy intermediate-scale quantum (NISQ) computing [68,69], a goal is to extract the maximum quantum computational power from the current devices. In the recent work on quantum supremacy [3], for a two-spin quantum gate, a fidelity value higher than 99% was achieved, but it decreases when the computing runs through multiple cycles. In our work, the noise effect is relatively severe due to the necessity to estimate derivatives from noisy time series. To partially reduce the noise, some basic signal processing techniques such as low-pass filtering can be exploited. Another method is to modify the loss function, since the noise is associated with the derivative term $\langle \dot{A}(t) \rangle_{\text{real}}$. For example, we can change it into a matrix form

$$\mathcal{L} = \sum_{\text{observations}} \|\dot{\mathbb{A}}^{(H)}(t)_{\text{real}} - \dot{\mathbb{A}}^{(H)}(t)_{\text{pred}}\|^2$$

and use matrix inversion to calculate $\mathbb{A}^{(H)}(t)$ and its time derivative $\dot{\mathbb{A}}^{(H)}(t)$. For matrix inversion, when the number of

initial states is sufficiently large, the computed matrix $\mathbb{A}^{(H)}(t)$ will converge to the true one. That is, the noise effect can be mitigated by taking more observations on linearly independent states for unbiased Gaussian noise.

The fourth issue is the numerical integration of Hamiltonian systems. In classical mechanics, the velocity field governing the Hamilton's equations of motion can be stiff, requiring unusually small time steps of integration to keep the numerical solutions stable [70]. In the literature, symplectic integrators guaranteeing the conservation of energy are often used to obtain numerical trajectories of Hamiltonian systems. The simplest symplectic integrator is the leapfrog method, also known as the Stömer-Verlet integrator [71]. However, even for the best integrators, severe forms of stiffness as characterized by mechanical rebounds or slingshot effects can compromise the numerical solutions. These issues represent a significant challenge in the development of learning algorithms based on the principles of Hamiltonian systems. Recently, symplectic recurrent neural networks (SRNNs) have been proposed [72]. For example, for the three-body problem, the SRNN-trained Hamiltonian is able to compensate for the discretization errors. The SRNNs can even outperform the symplectic methods for integrating Hamiltonian systems. In our work, the Baker-Campbell-Hausdorff formula was employed to convert the time-dependent Hamiltonian from the Heisenberg to the Schrödinger picture [73]. It is worthwhile to pursue extending the SRNN idea to quantum systems.

Recently, there have been efforts in understanding machine learning (the field of explainable machine learning), and physics-enhanced machine learning represents a useful perspective [74]. The HENN articulated in this paper, which includes time correlation, provides an effective way to ascertain and understand the hidden structures in the neural network. As such, our HENN may be exploited as a paradigm for explainable machine learning.

ACKNOWLEDGMENTS

This work was supported by the Air Force Office of Scientific Research through Grant No. FA9550-21-1-0438 and by the Army Research Office through Grant No. W911NF-21-2-0055.

APPENDIX A: EXAMPLES OF HEISENBERG NEURAL NETWORKS

We present a number of examples for which the HENN can be explicitly constructed.

1. One-spin system

The Hamiltonian of a single-spin system under a periodic driving is

$$H(t) = \sigma_x \sin(t). \quad (\text{A1})$$

We use the convention $\sigma_x = \sigma_+ + \sigma_-$ and $\sigma_y = i(-\sigma_+ + \sigma_-)$, where $\sigma_{+,-}$ correspond to the creation and annihilation operators, respectively. In the basis $|1\rangle$ and $|0\rangle$, the matrix

expressions of σ_x and σ_y are

$$\sigma_x = \begin{pmatrix} 0 & 1 \\ 1 & 0 \end{pmatrix} \quad \text{and} \quad \sigma_y = \begin{pmatrix} 0 & -i \\ i & 0 \end{pmatrix}. \quad (\text{A2})$$

The third spin operator is defined by $\sigma_z|1\rangle = |1\rangle$ and $\sigma_z|0\rangle = -|0\rangle$.

The HENN for the one-spin system can be constructed by following the three steps described in Sec. II as follows.

Step 1: We generate random initial conditions $|\psi_0\rangle$ given by

$$\psi_0 = \frac{1}{r_1 + r_2} \begin{pmatrix} \sqrt{r_1} \exp(i2\pi\theta_1) \\ \sqrt{r_2} \exp(i2\pi\theta_2) \end{pmatrix} = \begin{pmatrix} \phi_{11} + i\phi_{12} \\ \phi_{21} + i\phi_{22} \end{pmatrix}, \quad (\text{A3})$$

where $r_{1,2}$ are the initial probabilities in the respective state, $\theta_{1,2}$ are the corresponding phase variables, and both $r_{1,2}$ and

$\theta_{1,2}$ are uniform random numbers between 0 and 1. In the machine-learning algorithm, all quantities are real, so it is necessary to convert the wave function into the summation for the real and imaginary parts.

The time evolution of ψ_0 is governed by the Schrödinger equation. The expectation value of operator A is given by $\langle \psi_t | A | \psi_t \rangle$. In the Heisenberg picture, the states do not change but the operators change with time. We expand the operator $A^H(t)$ in the basis $|1\rangle$ and $|0\rangle$ with the corresponding matrix $\mathbb{A}^H(t)$. The Hermitian property of \mathbb{A}^H stipulates that it must contain four independent elements

$$\mathbb{A}^H(t) = \begin{pmatrix} A_1^H(t) & A_2^H(t) + iA_3^H(t) \\ A_2^H(t) - iA_3^H(t) & A_4^H(t) \end{pmatrix}. \quad (\text{A4})$$

Both the Schrödinger and Heisenberg pictures should give the same physical results. We have

$$(\phi_{11} - i\phi_{12}, \phi_{21} - i\phi_{22}) \begin{pmatrix} A_1^H(t) & A_2^H(t) + iA_3^H(t) \\ A_2^H(t) - iA_3^H(t) & A_4^H(t) \end{pmatrix} \begin{pmatrix} \phi_{11} + i\phi_{12} \\ \phi_{21} + i\phi_{22} \end{pmatrix} = \langle \psi_t | A | \psi_t \rangle. \quad (\text{A5})$$

The unknown elements $A^H(t)$ appear in the equation in a linear fashion:

$$A_1^H(t)(\phi_{11}^2 + \phi_{12}^2) + A_2^H(t)(2\phi_{11}\phi_{21} + 2\phi_{12}\phi_{22}) + A_3^H(t)(2\phi_{12}\phi_{21} - 2\phi_{11}\phi_{22}) + A_4^H(t)(\phi_{21}^2 + \phi_{22}^2) = \langle \psi_t | A | \psi_t \rangle. \quad (\text{A6})$$

At least four different initial conditions are required to solve this equation, and a further increase in the number of states changes the result only a little. We take A to be a Pauli matrix. Its expectation value versus time for a given initial state is illustrated in Fig. 7(a).

Step 2: Let the Hamiltonian of the unknown system be $H(t)$. The corresponding operator in the Heisenberg picture is $\mathbb{H}^H(t)$. Expanding the operator in the basis, we get

$$\mathbb{H}^H(t) = \begin{pmatrix} H_1^H(t) & H_2^H(t) + iH_3^H(t) \\ H_2^H(t) - iH_3^H(t) & H_4^H(t) \end{pmatrix}. \quad (\text{A7})$$

The quantum evolution is governed by the Heisenberg equation

$$\frac{dA^H(t)}{dt} = i[H^H(t), A^H(t)]. \quad (\text{A8})$$

For a given initial state, the Heisenberg equation can be written in matrix form as

$$\frac{d}{dt} \langle A \rangle_t = i\psi_0^\dagger [\mathbb{H}^H(t)\mathbb{A}^H(t) - \mathbb{A}^H(t)\mathbb{H}^H(t)]\psi_0. \quad (\text{A9})$$

Expanding the right side, we get a summation of 24 terms. As the system size is increased, the number in the summation grows quickly. Through the matrix product, we get

$$\frac{d}{dt} \langle A \rangle_t = \mathbb{T} \boldsymbol{\phi} \boldsymbol{\phi} \mathbf{A}(t) \mathbf{H}(t), \quad (\text{A10})$$

where

$$\begin{aligned} \boldsymbol{\phi} &= [\phi_{11}, \phi_{12}, \phi_{21}, \phi_{22}]^T, \\ \mathbf{A}(t) &= [A_1^H(t), A_2^H(t), A_3^H(t), A_4^H(t)]^T, \\ \mathbf{H}(t) &= [H_1^H(t), H_2^H(t), H_3^H(t), H_4^H(t)]^T, \end{aligned}$$

and \mathbb{T} is tensor of rank 4 (with dimension $4 \times 4 \times 4 \times 4$), which depends only on the dimension of the system and is defined as

$$\mathbb{T} \boldsymbol{\phi} \boldsymbol{\phi} \mathbf{A}(t) \mathbf{H}(t) = \sum_{i,j,m,n} \mathbb{T}_{ijmn} \phi_n \phi_m A_j(t) H_i(t). \quad (\text{A11})$$

The left side of Eq. (A9) contains the derivatives of the measurements, which can be determined from the observations. On the right side, $\mathbf{A}(t)$ and $\boldsymbol{\phi}$ are known, so the unknown quantity is $\mathbf{H}(t)$.

In the HENN, we set the input dimension as 1 and the output is $\mathbf{H}(t)$. We choose the batch size to be the number of measurement points times the number of different initial states. The loss function is

$$\mathcal{L} = \sum_{A=\sigma_x, \sigma_y, \sigma_z} |\langle \dot{A}(t) \rangle_{\text{real}} - \mathbb{T} \boldsymbol{\phi} \boldsymbol{\phi} \mathbf{A}(t) \mathbf{H}(t)|^2. \quad (\text{A12})$$

We build the neural network from the KERAS TENSORFLOW package [54], where the input is connected to two dense layers. Constructing this customized loss function is equivalent to designating a loss function with different weights.

Step 3: After the HENN is trained, we input a time series from 0 to 5 and predict the Hamiltonian. The prediction is carried out in the Heisenberg picture, which can be converted into the corresponding Hamiltonian in the Schrödinger picture. This can be done through an iteration process.

From the Hamiltonian in the Schrödinger picture, we can get the coefficients in each base through

$$H(t) = c_0(t)\mathbb{I}_2 + c_1(t)\sigma_x + c_2(t)\sigma_y + c_3(t)\sigma_z. \quad (\text{A13})$$

Writing it in a general form $H(t) = \sum_i S_i c_i(t)$, where $S = \mathbb{I}_2, \sigma_x, \sigma_y, \sigma_z$, we have that $c_i(t)$'s contain all the information about the Hamiltonian. The predicted $c_i(t)$ in a given basis are

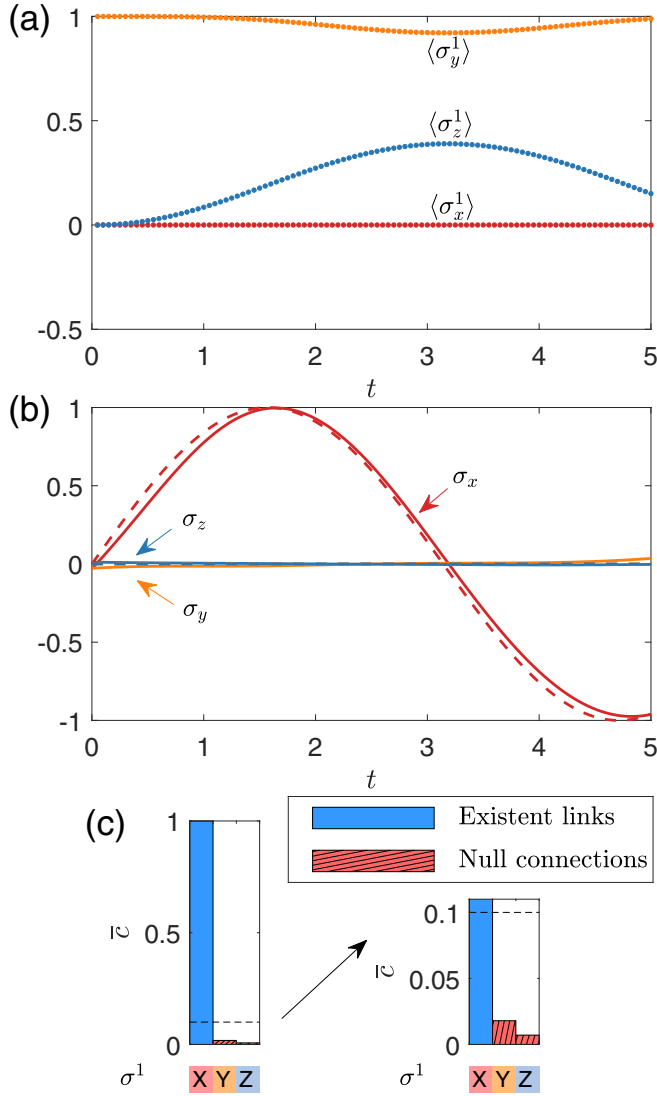


FIG. 7. HENN-based tomography of a single-spin system. (a) Time series of σ_x , σ_y , and σ_z , where the initial state is $(|1\rangle + i|0\rangle)/\sqrt{2}$. The dots correspond to the sampled measurements. (b) The predicted Hamiltonian in the Schrödinger picture, where the three curves correspond to the decomposition in the three base states, and the dashed curves are the true values. (c) Time average of the absolute value of $c_i(t)$ in different base states. The existent links are marked by the solid blue bars, and the nonexistent ones by the red bars with parallel lines, where the threshold for determining the existent links is 10% of the maximum value.

shown Fig. 7(b). The agreement between the solid (predicted) and dashed (true) curves is proof that the HENN can recover the Hamiltonian of the original system through observations.

The coupling configuration can be determined through

$$\bar{c}_i = \int |c_i(t)| dt. \quad (\text{A14})$$

If there exists a coupling between the spin components, the corresponding coefficient $c_i(t)$ should be nonzero, giving rise to a nonzero value of \bar{c}_i . Figure 7(c) shows the time-averaged result of $c_i(t)$, which has a pronounced value in σ_x , in agreement with the original Hamiltonian (A1).

2. A three-spin chain

We consider three interacting spins on a chain, with measurements taken from the first spin, as shown in Fig. 8. The Hamiltonian is

$$H(t) = \sin(t) \left(\sum_{i=1}^3 \sum_{j=1}^2 \sigma_j^i + \sum_{i=1}^2 \sum_{l=1}^3 \sum_{m=1}^2 \sigma_l^i \sigma_m^{i+1} \right). \quad (\text{A15})$$

There are couplings between spins 1 and 2, and between spins 2 and 3. For each coupling, there are six links.

The HENN can be constructed following the three steps.

Step 1: The system contains 2^3 independent states: $|111\rangle, |110\rangle, |011\rangle, \dots, |000\rangle$. The initial conditions are chosen according to Eq. (A3), with the difference that here there are eight dimensions. Since observations are taken from the first spin, we write $\sigma_x^1 = \sigma_+^1 + \sigma_-^1$, where the creation and annihilation operators act only on the first spin. The matrix expression for σ_x^1 is

$$\sigma_x^1 = \sigma_x \otimes \mathbb{I}_4.$$

Similarly, we can get the matrices for σ_y^1 and σ_z^1 . For a given initial state, we calculate the expectation values of the three observables on the first spin, as shown in Fig. 8(b).

Step 2: Similar to the one-spin system, the Heisenberg equation is

$$\frac{d}{dt} \langle A \rangle_t = \mathbb{T} \phi \phi \mathbf{A}(t) \mathbf{H}(t), \quad (\text{A16})$$

where ϕ is a vector of $2 \times 2^3 = 16$ elements, $\mathbf{A}(t)$ and $\mathbf{H}(t)$ contain $4^3 = 64$ elements, and \mathbb{T} is a tensor of rank 4 with the dimension $64 \times 64 \times 16 \times 16$:

$$\mathbb{T} \phi \phi \mathbf{A}(t) \mathbf{H}(t) = \sum_{i,j,m,n} \mathbb{T}_{ijmn} \phi_n \phi_m A_j(t) H_i(t). \quad (\text{A17})$$

We build up the HENN according to the same loss function as in the case of a single-spin system, predict the Hamiltonian, and convert it to the Schrödinger picture. The Hamiltonian can be decomposed as

$$\begin{aligned} \mathbb{H}(t) = & c_0(t) \mathbb{I} + \sum_{i,j} c_{i,j}(t) \sigma_j^i + \sum_{i,j,m,n} c_{ijmn}(t) \sigma_j^i \sigma_n^m \\ & + \sum_{i,j,m,n,k,l} c_{ijmnlk}(t) \sigma_j^i \sigma_n^m \sigma_l^k. \end{aligned} \quad (\text{A18})$$

The decomposition becomes cumbersome for systems with more than one spin. We thus write this as the direct product of the Pauli matrices plus the identity matrix. For example, the two-body coupling $\sigma_1^1 \sigma_2^2$ can be written as $\sigma_1^1 \otimes \sigma_2^2 \otimes \sigma_0^3$.

Figure 8(c) shows the predicted Hamiltonian in several base states. The Hamiltonian for the coupling $\sigma_x^1 \sigma_x^2$ can be compared with the sinusoidal function $\sin(t)$. The coupling term $\sigma_x^1 \sigma_x^3$ is nonexistent in the original system, so it should be compared with zero. The agreement indicates that the local Hamiltonian between the observed spin and the nonobservable spins can be recovered. Note that $\sigma_x^2 \sigma_x^3$ represents a coupling between the two nonobservable nodes, whose true value is $\sin(t)$, but the predicted Hamiltonian is not close to it. Nonetheless, the nonzero value of the predicted term indicates the existence of the coupling term $\sigma_x^2 \sigma_x^3$.

Step 3: After decomposing the Hamiltonian in different terms, we take the time average of each and normalize them, as shown in Fig. 8(d). The ideal case is that all the true interactions have the value 1, and all the nonexistent couplings

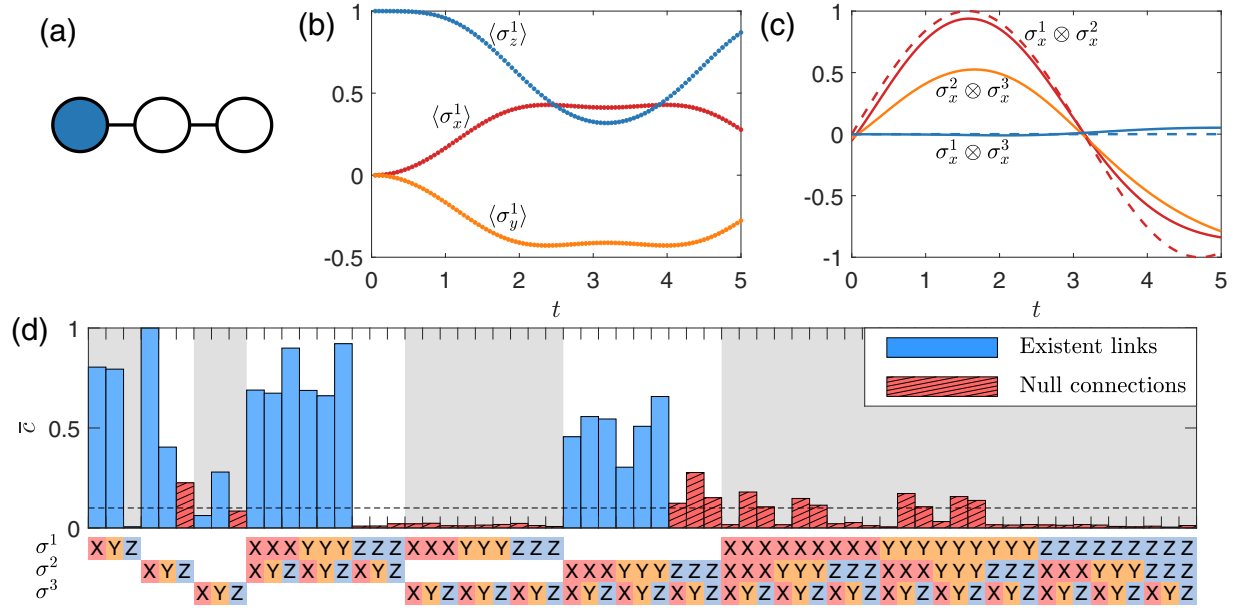


FIG. 8. HENN-based tomography of a three-spin chain system. (a) Schematic illustration of the chain, where measurements are taken from the left spin. (b) Time series of σ_x^1 , σ_y^1 , and σ_z^1 from the initial state $\frac{|1\rangle+|0\rangle}{\sqrt{2}}|11\rangle$, where the dots correspond to the sampled measurement time series. (c) Predicted Hamiltonian in the Schrödinger picture after decomposition into different interaction terms, where $\sigma_x^1 \otimes \sigma_x^2$ and $\sigma_x^1 \otimes \sigma_x^3$ are the couplings between the observed node and the nonobservable nodes, which agree with the true Hamiltonian terms (dashed traces). The term $\sigma_x^2 \otimes \sigma_x^3$ specifies the coupling between the two nonobservable nodes, and the predicted Hamiltonian is not similar to the true function $\sin(t)$ but is not zero either, so the HENN does predict the existence of this interaction. (d) Time average of the absolute value of the coefficients $c_i(t)$ associated with different interaction terms, where the existent links are marked by filled blue bars, and the nonexistent ones by red bars with parallel lines. The threshold for distinguishing the existent from the nonexistent links is set to be 10% of the maximum coefficient value, as indicated by the horizontal dashed line.

correspond to 0. First, the Hamiltonian Eq. (A15) contains self-couplings in x and y but not in z , which are indicated by the first three bars in Fig. 8(d). For the nonobservable spins, there are errors in predicting the self-coupling terms. Second, there are two-body interactions between spins 1 and 2, and between spins 2 and 3, but not between 1 and 3, where each existent interaction has six terms of coupling. The predicted results for the couplings involving the first spin are more accurate than those between the nonobservable spins. Third, the true Hamiltonian does not include any three-body interactions, so all such terms should be zero.

The results in Fig. 8 indicate that our HENN can perform accurate tomography of the three-spin chain.

APPENDIX B: TIME-INDEPENDENT TOFFOLI AND FREDKIN GATES

The Hamiltonian for the time-independent Toffoli gate is

$$H_{\text{Toffoli}} = \frac{\pi}{8} (\mathbb{I}_2 - \sigma_3^1) (\mathbb{I}_2 - \sigma_3^2) (\mathbb{I}_2 - \sigma_1^3). \quad (\text{B1})$$

The corresponding time evolution operator is

$$U_{\text{Toffoli}} = \begin{pmatrix} \mathbb{I}_6 & \\ & \mathbb{X}_0(t) \end{pmatrix}, \quad (\text{B2})$$

where

$$\mathbb{X}_0(t) = \frac{1}{2} \begin{pmatrix} 1 + \exp(i\pi t) & 1 - \exp(i\pi t) \\ 1 - \exp(i\pi t) & 1 + \exp(i\pi t) \end{pmatrix}. \quad (\text{B3})$$

The Hamiltonian for the time-independent Fredkin gate is

$$H_{\text{Fredkin}} = \frac{\pi}{8} (\mathbb{I}_2 - \sigma_3^1) \left[\mathbb{I}_4 - \sum_{\alpha=1}^3 \sigma_\alpha^2 \sigma_\alpha^3 \right], \quad (\text{B4})$$

with

$$U_{\text{Fredkin}} = \begin{pmatrix} \mathbb{I}_5 & & \\ & \mathbb{X}_0(t) & \\ & & 1 \end{pmatrix}. \quad (\text{B5})$$

- [1] M. A. Nielsen and I. Chuang, *Quantum Computation and Quantum Information* (Cambridge University Press, Cambridge, England, 2000).
- [2] C. Neill, P. Roushan, K. Kechedzhi, S. Boixo, S. V. Isakov, V. Smelyanskiy, A. Megrant, B. Chiaro, A. Dunsworth, K. Arya *et al.*, A blueprint for demonstrating quantum supremacy with superconducting qubits, *Science* **360**, 195 (2018).

- [3] F. Arute, K. Arya, R. Babbush, D. Bacon, J. C. Bardin, R. Barends, R. Biswas, S. Boixo, F. G. Brandao, D. A. Buell *et al.*, Quantum supremacy using a programmable superconducting processor, *Nature (London)* **574**, 505 (2019).
- [4] B. Yurke and J. S. Denker, Quantum network theory, *Phys. Rev. A* **29**, 1419 (1984).

- [5] J. I. Cirac, P. Zoller, H. J. Kimble, and H. Mabuchi, Quantum State Transfer and Entanglement Distribution Among Distant Nodes in a Quantum Network, *Phys. Rev. Lett.* **78**, 3221 (1997).
- [6] M. Christandl, N. Datta, A. Ekert, and A. J. Landahl, Perfect State Transfer in Quantum Spin Networks, *Phys. Rev. Lett.* **92**, 187902 (2004).
- [7] A. S. Parkins, P. Marte, P. Zoller, and H. J. Kimble, Synthesis of Arbitrary Quantum States Via Adiabatic Transfer of Zeeman Coherence, *Phys. Rev. Lett.* **71**, 3095 (1993).
- [8] L.-M. Duan and C. Monroe, Colloquium: Quantum networks with trapped ions, *Rev. Mod. Phys.* **82**, 1209 (2010).
- [9] A. Barenco, C. H. Bennett, R. Cleve, D. P. DiVincenzo, N. Margolus, P. Shor, T. Sleator, J. A. Smolin, and H. Weinfurter, Elementary gates for quantum computation, *Phys. Rev. A* **52**, 3457 (1995).
- [10] D. Aharonov, W. Van Dam, J. Kempe, Z. Landau, S. Lloyd, and O. Regev, Adiabatic quantum computation is equivalent to standard quantum computation, *SIAM Rev.* **50**, 755 (2008).
- [11] S. C. Benjamin and S. Bose, Quantum Computing with an Always-On Heisenberg Interaction, *Phys. Rev. Lett.* **90**, 247901 (2003).
- [12] D. Burgarth, K. Maruyama, M. Murphy, S. Montangero, T. Calarco, F. Nori, and M. B. Plenio, Scalable quantum computation via local control of only two qubits, *Phys. Rev. A* **81**, 040303(R) (2010).
- [13] E. Sjöqvist, D.-M. Tong, L. M. Andersson, B. Hessmo, M. Johansson, and K. Singh, Non-adiabatic holonomic quantum computation, *New J. Phys.* **14**, 103035 (2012).
- [14] S. J. Glaser, U. Boscain, T. Calarco, C. P. Koch, W. Köckenberger, R. Kosloff, I. Kuprov, B. Luy, S. Schirmer, T. Schulte-Herbrüggen *et al.*, Training Schrödinger's cat: quantum optimal control, *Eur. Phys. J. D* **69**, 279 (2015).
- [15] L. Banchi, N. Pancotti, and S. Bose, Quantum gate learning in qubit networks: Toffoli gate without time-dependent control, *npj Quantum Inf.* **2**, 16019 (2016).
- [16] L. Innocenti, L. Banchi, A. Ferraro, S. Bose, and M. Paternostro, Supervised learning of time-independent Hamiltonians for gate design, *New J. Phys.* **22**, 065001 (2020).
- [17] S. Ahmed, C. S. Munoz, F. Nori, and A. F. Kockum, Quantum State Tomography with Conditional Generative Adversarial Networks, *Phys. Rev. Lett.* **127**, 140502 (2021).
- [18] S. Ahmed, C. S. Munoz, F. Nori, and A. F. Kockum, Classification and reconstruction of optical quantum states with deep neural networks, *Phys. Rev. Res.* **3**, 033278 (2021).
- [19] J. Zhang and M. Sarovar, Quantum Hamiltonian Identification from Measurement Time Traces, *Phys. Rev. Lett.* **113**, 080401 (2014).
- [20] J. Zhang and M. Sarovar, Identification of open quantum systems from observable time traces, *Phys. Rev. A* **91**, 052121 (2015).
- [21] A. Shabani, M. Mohseni, S. Lloyd, R. L. Kosut, and H. Rabitz, Estimation of many-body quantum Hamiltonians via compressive sensing, *Phys. Rev. A* **84**, 012107 (2011).
- [22] E. Magesan, A. Cooper, and P. Cappellaro, Compressing measurements in quantum dynamic parameter estimation, *Phys. Rev. A* **88**, 062109 (2013).
- [23] Z. Li, L. Zou, and T. H. Hsieh, Hamiltonian Tomography Via Quantum Quench, *Phys. Rev. Lett.* **124**, 160502 (2020).
- [24] L. E. De Clercq, R. Oswald, C. Flühmann, B. Keitch, D. Kienzler, H.-Y. Lo, M. Marinelli, D. Nadlinger, V. Negnevitsky, and J. P. Home, Estimation of a general time-dependent Hamiltonian for a single qubit, *Nat. Commun.* **7**, 11218 (2016).
- [25] E. Bairey, I. Arad, and N. H. Lindner, Learning a Local Hamiltonian from Local Measurements, *Phys. Rev. Lett.* **122**, 020504 (2019).
- [26] J. Unger, S. Dong, R. Flores, Q. Su, and R. Grobe, Infinite-dimensional optimization applied to pair creation from the vacuum, *Phys. Rev. A* **99**, 022128 (2019).
- [27] D. Zhao, C. Wei, S. Xue, Y. Huang, X. Nie, J. Li, D. Ruan, D. Lu, T. Xin, and G. Long, Characterizing quantum simulations with quantum tomography on a spin quantum simulator, *Phys. Rev. A* **103**, 052403 (2021).
- [28] A. A. Gentile, B. Flynn, S. Knauer, N. Wiebe, S. Paesani, C. E. Granade, J. G. Rarity, R. Santagati, and A. Laing, Learning models of quantum systems from experiments, *Nat. Phys.* **17**, 837 (2021).
- [29] G. Carleo, I. Cirac, K. Cranmer, L. Daudet, M. Schuld, N. Tishby, L. Vogt-Maranto, and L. Zdeborová, Machine learning and the physical sciences, *Rev. Mod. Phys.* **91**, 045002 (2019).
- [30] P. De Wilde, Class of Hamiltonian neural networks, *Phys. Rev. E* **47**, 1392 (1993).
- [31] S. Greydanus, M. Dzamba, and J. Yosinski, Hamiltonian neural networks, *arXiv:1906.01563*.
- [32] T. Bertalan, F. Dietrich, I. Mezić, and I. G. Kevrekidis, On learning Hamiltonian systems from data, *Chaos* **29**, 121107 (2019).
- [33] A. Choudhary, J. F. Lindner, E. G. Holliday, S. T. Miller, S. Sinha, and W. L. Ditto, Physics-enhanced neural networks learn order and chaos, *Phys. Rev. E* **101**, 062207 (2020).
- [34] C.-D. Han, B. Glaz, M. Haile, and Y.-C. Lai, Adaptable Hamiltonian neural networks, *Phys. Rev. Res.* **3**, 023156 (2021).
- [35] M. Timme, Revealing Network Connectivity from Response Dynamics, *Phys. Rev. Lett.* **98**, 224101 (2007).
- [36] S. G. Shandilya and M. Timme, Inferring network topology from complex dynamics, *New J. Phys.* **13**, 013004 (2011).
- [37] R.-Q. Su, W.-X. Wang, and Y.-C. Lai, Detecting hidden nodes in complex networks from time series, *Phys. Rev. E* **85**, 065201(R) (2012).
- [38] X. Han, Z. Shen, W.-X. Wang, and Z. Di, Robust Reconstruction of Complex Networks from Sparse Data, *Phys. Rev. Lett.* **114**, 028701 (2015).
- [39] W.-X. Wang, Y.-C. Lai, and C. Grebogi, Data based identification and prediction of nonlinear and complex dynamical systems, *Phys. Rep.* **644**, 1 (2016).
- [40] Y. Kato and N. Yamamoto, Structure identification and state initialization of spin networks with limited access, *New J. Phys.* **16**, 023024 (2014).
- [41] C. Di Franco, M. Paternostro, and M. S. Kim, Hamiltonian Tomography in an Access-Limited Setting Without State Initialization, *Phys. Rev. Lett.* **102**, 187203 (2009).
- [42] N. A. Peters, J. T. Barreiro, M. E. Goggin, T.-C. Wei, and P. G. Kwiat, Remote State Preparation: Arbitrary Remote Control of Photon Polarization, *Phys. Rev. Lett.* **94**, 150502 (2005).
- [43] X.-Q. Xiao, J.-M. Liu, and G. Zeng, Joint remote state preparation of arbitrary two- and three-qubit states, *J. Phys. B* **44**, 075501 (2011).
- [44] P. J. Shadbolt, M. R. Verde, A. Peruzzo, A. Politi, A. Laing, M. Lobino, J. C. Matthews, M. G. Thompson, and J. L. O'Brien,

- Generating, manipulating and measuring entanglement and mixture with a reconfigurable photonic circuit, *Nat. Photon.* **6**, 45 (2012).
- [45] I. L. Chuang and M. A. Nielsen, Prescription for experimental determination of the dynamics of a quantum black box, *J. Mod. Opt.* **44**, 2455 (1997).
- [46] S. T. Merkel, J. M. Gambetta, J. A. Smolin, S. Poletto, A. D. Córcoles, B. R. Johnson, C. A. Ryan, and M. Steffen, Self-consistent quantum process tomography, *Phys. Rev. A* **87**, 062119 (2013).
- [47] J. L. O'Brien, G. J. Pryde, A. Gilchrist, D. F. V. James, N. K. Langford, T. C. Ralph, and A. G. White, Quantum Process Tomography of a Controlled-Not Gate, *Phys. Rev. Lett.* **93**, 080502 (2004).
- [48] M. Riebe, K. Kim, P. Schindler, T. Monz, P. O. Schmidt, T. K. Körber, W. Hänsel, H. Häffner, C. F. Roos, and R. Blatt, Process Tomography of Ion Trap Quantum Gates, *Phys. Rev. Lett.* **97**, 220407 (2006).
- [49] T. Monz, K. Kim, W. Hänsel, M. Riebe, A. S. Villar, P. Schindler, M. Chwalla, M. Hennrich, and R. Blatt, Realization of the Quantum Toffoli Gate with Trapped Ions, *Phys. Rev. Lett.* **102**, 040501 (2009).
- [50] L. Che, C. Wei, Y. Huang, D. Zhao, S. Xue, X. Nie, J. Li, D. Lu, and T. Xin, Learning quantum Hamiltonians from single-qubit measurements, *Phys. Rev. Res.* **3**, 023246 (2021).
- [51] A. H. Myerson, D. J. Szwer, S. C. Webster, D. T. C. Allcock, M. J. Curtis, G. Imreh, J. A. Sherman, D. N. Stacey, A. M. Steane, and D. M. Lucas, High-Fidelity Readout of Trapped-Ion Qubits, *Phys. Rev. Lett.* **100**, 200502 (2008).
- [52] J. M. Chow, L. DiCarlo, J. M. Gambetta, A. Nunnenkamp, L. S. Bishop, L. Frunzio, M. H. Devoret, S. M. Girvin, and R. J. Schoelkopf, Detecting highly entangled states with a joint qubit readout, *Phys. Rev. A* **81**, 062325 (2010).
- [53] M. Neeley, R. C. Bialczak, M. Lenander, E. Lucero, M. Mariantoni, A. O'Connell, D. Sank, H. Wang, M. Weides, J. Wenner *et al.*, Generation of three-qubit entangled states using superconducting phase qubits, *Nature (London)* **467**, 570 (2010).
- [54] F. Chollet *et al.*, Keras, <https://keras.io>.
- [55] D. P. Kingma and J. Ba, Adam: A method for stochastic optimization, [arXiv:1412.6980](https://arxiv.org/abs/1412.6980).
- [56] R. J. Baxter, *Exactly Solved Models in Statistical Mechanics* (Elsevier, Amsterdam, 2016).
- [57] H. Nishimori, *Statistical Physics of Spin Glasses and Information Processing: An Introduction* (Oxford University Press, Oxford, 2001).
- [58] E. Fredkin and T. Toffoli, Conservative logic, *Int. J. Theor. Phys.* **21**, 219 (1982).
- [59] L. DiCarlo, M. D. Reed, L. Sun, B. R. Johnson, J. M. Chow, J. M. Gambetta, L. Frunzio, S. M. Girvin, M. H. Devoret, and R. J. Schoelkopf, Preparation and measurement of three-qubit entanglement in a superconducting circuit, *Nature (London)* **467**, 574 (2010).
- [60] B. P. Lanyon, M. Barbieri, M. P. Almeida, T. Jennewein, T. C. Ralph, K. J. Resch, G. J. Pryde, J. L. O'Brien, A. Gilchrist, and A. G. White, Simplifying quantum logic using higher-dimensional Hilbert spaces, *Nat. Phys.* **5**, 134 (2009).
- [61] R. B. Patel, J. Ho, F. Ferreyrol, T. C. Ralph, and G. J. Pryde, A quantum Fredkin gate, *Sci. Adv.* **2**, e1501531 (2016).
- [62] A. Fedorov, L. Steffen, M. Baur, M. P. da Silva, and A. Wallraff, Implementation of a Toffoli gate with superconducting circuits, *Nature (London)* **481**, 170 (2012).
- [63] D. Burgarth, K. Maruyama, and F. Nori, Coupling strength estimation for spin chains despite restricted access, *Phys. Rev. A* **79**, 020305(R) (2009).
- [64] E. H. Lapasar, K. Maruyama, D. Burgarth, T. Takui, Y. Kondo, and M. Nakahara, Estimation of coupling constants of a three-spin chain: a case study of Hamiltonian tomography with nuclear magnetic resonance, *New J. Phys.* **14**, 013043 (2012).
- [65] A. Sone and P. Cappellaro, Exact dimension estimation of interacting qubit systems assisted by a single quantum probe, *Phys. Rev. A* **96**, 062334 (2017).
- [66] H. Haehne, J. Casadiego, J. Peinke, and M. Timme, Detecting Hidden Units and Network Size from Perceptible Dynamics, *Phys. Rev. Lett.* **122**, 158301 (2019).
- [67] N. Shazeer, A. Mirhoseini, K. Maziarz, A. Davis, Q. Le, G. Hinton, and J. Dean, Outrageously large neural networks: The sparsely-gated mixture-of-experts layer, [arXiv:1701.06538](https://arxiv.org/abs/1701.06538).
- [68] J. Preskill, Quantum computing in the NISQ era and beyond, *Quantum* **2**, 79 (2018).
- [69] K. Bharti, A. Cervera-Lierta, T. H. Kyaw, T. Haug, S. Alperin-Lea, A. Anand, M. Degroote, H. Heimonen, J. S. Kottmann, T. Menke *et al.*, Noisy intermediate-scale quantum (NISQ) algorithms, [arXiv:2101.08448](https://arxiv.org/abs/2101.08448).
- [70] J. D. Lambert *et al.*, *Numerical Methods for Ordinary Differential Systems* (Wiley, New York, 1991), Vol. 146.
- [71] B. Leimkuhler and S. Reich, *Simulating Hamiltonian Dynamics* (Cambridge University Press, Cambridge, England, 2004).
- [72] Z. Chen, J. Zhang, M. Arjovsky, and L. Bottou, Symplectic recurrent neural networks, [arXiv:1909.13334](https://arxiv.org/abs/1909.13334).
- [73] J. J. Sakurai and E. D. Commins, *Modern Quantum Mechanics* (Addison-Wesley, Reading, MA, 1995).
- [74] R. Iten, T. Metger, H. Wilming, L. del Rio, and R. Renner, Discovering Physical Concepts with Neural Networks, *Phys. Rev. Lett.* **124**, 010508 (2020).